

Cite this: *RSC Adv.*, 2017, 7, 53925

# Ultrasensitive room-temperature ethanol detection based on Au functionalized nanoporous SnO<sub>2</sub>/C<sub>60</sub>/SnO<sub>2</sub> composites†

Shaofeng Shao,<sup>ID</sup>\*<sup>a</sup> Wei Wang,<sup>a</sup> Yunyun Chen,<sup>a</sup> Yunfei Wang<sup>a</sup> and Ralf Koehn<sup>b</sup>

We have realized extremely sensitive, selective sub-ppm level ethanol gas detection through an Au functionalized nanoporous SnO<sub>2</sub>/C<sub>60</sub>/SnO<sub>2</sub> sensing composite. This new type of hierarchically nanoporous SnO<sub>2</sub> composite film supports both the Au@SnO<sub>2</sub>/C<sub>60</sub> layer with closely packed open macropores (~300 nm) and the bottom SnO<sub>2</sub> layer with highly ordered nanopores (8–10 nm). The structure, crystallinity and composition of the hierarchical structured Au@SnO<sub>2</sub>/C<sub>60</sub>/SnO<sub>2</sub> nanocomposite films are characterized by XRD, Raman, HRTEM, and SAED. The interaction between the Au/SnO<sub>2</sub> and C<sub>60</sub>/SnO<sub>2</sub> heterojunctions in light of transfer of charge carriers and modulation of potential barriers plays a crucial role in enhancing the detecting performance. The sensing properties of the Au@SnO<sub>2</sub>/C<sub>60</sub>/SnO<sub>2</sub> nanocomposite sensor are investigated by exposing it to ethanol gas with a concentration range from 0.5 ppm to 50 ppm. Furthermore, the gas sensor exhibits ultrahigh sensitivity to ethanol gas with a response value of up to 16.8 at 0.5 ppm and a short recovery time of 9 seconds at room temperature.

Received 7th October 2017  
Accepted 16th November 2017

DOI: 10.1039/c7ra11021a

rsc.li/rsc-advances

## 1. Introduction

Ethanol as one of the most commonly and widely used chemical compounds, is applied in many fields such as the chemical industry, medicine, and the food industry. Furthermore, ethanol fuel is also a clean, efficient, and promising candidate for a renewable energy source that will overcome current challenges such as air pollution and the global energy crisis. In this growing ethanol fuel economy, safety challenges involving ethanol production, transportation, and storage require precise quantitative detection of ethanol vapour at sub-ppm level. Besides 1D nanomaterials,<sup>1</sup> hollow spheres,<sup>2</sup> and core-shell materials,<sup>3</sup> ordered nanoporous SnO<sub>2</sub> based sensors have undergone extensive development, because they usually offer acceptable sensing performance due to large active surface area and efficient gas diffusion induction. However, they suffered from an obvious drawback of high operating temperature, resulting in high power consumption and difficulty in integration.<sup>4</sup> Therefore, the design and synthesis of effective materials and devices for high sensing performance at room temperature are of crucial important for practical applications.

Recently, SnO<sub>2</sub> decorated with nanoscale carbon materials such as carbon nanotube, graphene, and fullerene have attracted much attention for gas sensor.<sup>5–7</sup> In particular, C<sub>60</sub> appears to be attractive for its special electric property because it is chemically stable, metallic impurity free and relatively simple to implement and gives rise to reproducible electrical responses.<sup>8,9</sup> Zito *et al.* synthesized the C–SnO<sub>2</sub> nanocomposite forming p/n heterojunction to get enhanced sensing performance for ethanol gas. It was proposed that the formation of p/n junction was responsible for the improved sensing performance of SnO<sub>2</sub> based sensing materials.<sup>10</sup> Qu *et al.* reported porous C<sub>60</sub>/SnO<sub>2</sub> composites exhibited high sensitivity to 5 ppm ethanol gas with operating temperature 100 °C.<sup>11</sup> However, C<sub>60</sub>-based sensors with p/n heterojunction still had some disadvantages in modifying the diffusion and adsorption of gas molecules on the sensing materials surface, which led to the long response–recovery time. The response time to 5 ppm ethanol gas was as long as 100 second. For improving the response performance, Nguyet *et al.* fabricated n–p–n heterojunctions of C/SnO<sub>2</sub> nanowires to obtain high enhancement in gas sensing performance.<sup>12</sup> Therefore, the n/p/n heterojunction between SnO<sub>2</sub> nanoparticles and C<sub>60</sub> on the porous nanostructure would be able to enhance the ability of the gas molecules to diffuse and adsorb on the sensing materials, thus promoting the sensor performance.

On the other hand, several strategies demonstrated that the incorporation metal nanoparticles such as Au, Pt, Pd, and Ag to the metal oxides surface can effectively reduce the operating temperature and improve the lower limit detection, sensor

<sup>a</sup>Jiangsu Key Laboratory for Optoelectronic Detection of Atmosphere and Ocean, Nanjing University of Information Science & Technology, Nanjing, China. E-mail: ssfshao@uist.edu.cn; Fax: +86-25-58731031; Tel: +86-25-58731031

<sup>b</sup>Center for Free-Electron Laser Science, Building 99, Notkestrasse 85, Hamburg, Germany

† Electronic supplementary information (ESI) available. See DOI: 10.1039/c7ra11021a

response, sensitivity, and selectivity.<sup>13–16</sup> Au nanoparticles have received the most attention from the scientific community, especially for sensor applications, because of their chemical inertness, high adsorption, and excellent catalytic activity,<sup>17–20</sup> where the Au modified  $\text{SnO}_2/\text{C}_{60}/\text{SnO}_2$  nanocomposite film based gas sensor can be exploited to detect ethanol gas at room temperature.

In the present work, we synthesize nanoporous  $\text{SnO}_2/\text{C}_{60}/\text{SnO}_2$  sensing film decorated with Au applying the water vapour post-synthetic hydrothermal treatment, in order to form n/p/n heterojunction for improving sensing behaviour. This new type of hierarchically nanoporous  $\text{SnO}_2$  composite films supporting both the  $\text{Au@SnO}_2/\text{C}_{60}$  layer with closely packed open macropores ( $\sim 300$  nm) and the bottom  $\text{SnO}_2$  layer with highly ordered nanopores (8–10 nm). The generation of p/n heterojunctions between  $\text{C}_{60}/\text{SnO}_2$  nanoparticles can inevitably develop the depletion regions of the junction, decreasing the conduction volume of  $\text{SnO}_2$  nanoparticles. Furthermore, the potential barrier (0.17 eV) between  $\text{SnO}_2/\text{C}_{60}/\text{SnO}_2$  heterojunction will be developed at both sides of n/p/n heterojunctions, being accompanied by the bending of the vacuum energy level and the energy band. Therefore, the  $\text{SnO}_2/\text{C}_{60}/\text{SnO}_2$  heterojunctions will provide additional modulation of resistance during the introduction and removal of ethanol gas by changing the n/p/n heterojunction barrier. The addition of Au catalyst will provide a great significant effect on the enhancement of sensing performance. By the spill over effect, the target gas molecules will be efficiently adsorbed on Au surface. They can be easily transported to the adjacent  $\text{SnO}_2$  surface.<sup>21</sup> On the other hand, the Schottky barriers (0.55 eV) generated at Au– $\text{SnO}_2$  heterojunctions will provide additional modulation of resistance during the adsorption and desorption of ethanol gas by changing the heterojunction barrier. For hierarchical  $\text{Au@SnO}_2/\text{C}_{60}/\text{SnO}_2$  composite film, we obtain remarkable development of ethanol sensors, and the sensor response is up to 16.8 for 0.5 ppm ethanol gas, which is a prominent result in terms of ethanol detection at room temperature.

## 2. Experimental section

### 2.1 Experimental methods

#### Step 1: ordered nanoporous $\text{SnO}_2$ sensing film fabrication.

Experimental procedures are described in Fig. 1. The Sn precursor solution was prepared by dissolving 100 mg  $\text{SnCl}_4$  (Aldrich, >99%) in 0.016 mol ethanol (>99.5%) in the presence of  $4.0 \times 10^{-6}$  mol Pluronic F127 triblock copolymer (Sigma, BioReagent). 0.1 ml 12 M HCl (37 wt%) was then mixed with the above tin precursor solution under constant stirring for overnight. The resulting precursor solution was stable over one month period. The molar ratio of Sn : F127 : EtOH : HCl :  $\text{H}_2\text{O}$  in the final Sn precursor solution was 1 : 0.01 : 40 : 3 : 10. The thin films were prepared by spin-coating 50  $\mu\text{l}$  of the Sn precursor solution onto one sensor device of  $\text{ca. } 10 \times 10 \text{ mm}^2$  with interdigital electrode at 4000 rpm for 30 s under 30% relative humidity for five times, and then dried at 60 °C for 2 h. The films were then exposed to a water vapour hydrothermal treatment, 80% relative humidity, at 100 °C for 96 h. The relative

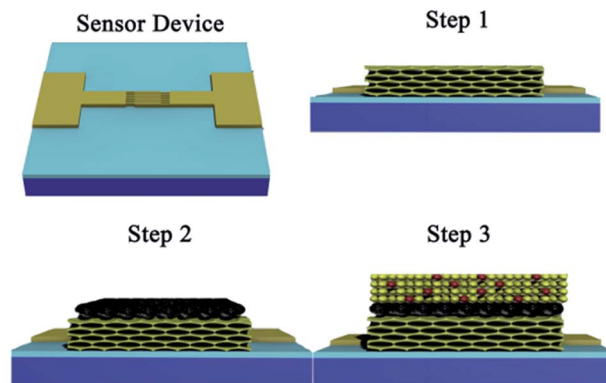


Fig. 1 Schematic illustration of the fabrication for  $\text{Au@SnO}_2/\text{C}_{60}/\text{SnO}_2$  sensing film based on the sensor device.

humidity was achieved using a supersaturated salt aqueous solution, kept at 100 °C, in a humidity controlled chamber. The films were then heat treated by annealing at temperature of 300 °C for 2 h with an up/down ramp rate of 1.0 °C  $\text{min}^{-1}$ . In Fig. 1, the step 1 shows the ordered nanoporous  $\text{SnO}_2$  thin film on the sensor device.

**Step 2:  $\text{C}_{60}/\text{SnO}_2$  sensing film fabrication.** The  $\text{C}_{60}$  solution was prepared by adding 5 mg  $\text{C}_{60}$  (Aldrich, >99.5%) in 0.016 mol ethanol (>99.5%) in the presence of  $3.6 \times 10^{-6}$  mol Pluronic F127 triblock copolymer (Sigma, BioReagent), and then dropped in 50  $\mu\text{l}$  12 M HCl (37 wt%) with the aid of ultrasound for 5 minutes. The mixture was then under constant stirring for overnight. Composite films were synthesized by spin-coating 40  $\mu\text{l}$  of the  $\text{C}_{60}$  precursor solution on one above sensor device with ordered nanoporous  $\text{SnO}_2$  thin film (Fig. 1 step 1) at 4000 rpm for 60 seconds under 30% relative humidity for two times, and then dried at 60 °C for one hour. The nanocomposite thin films were then oxygen-plasma treated (Femto, 40 kHz, 100 W) for 4 minutes.

**Step 3:  $\text{Au@SnO}_2/\text{C}_{60}/\text{SnO}_2$  sensing film fabrication.**  $\text{Au@SnO}_2/\text{C}_{60}/\text{SnO}_2$  sensing thin film was fabricated through a simple route. The Au–Sn precursor solutions were prepared by dissolving 100 mg  $\text{SnCl}_4$  (Aldrich, >99%) in 0.016 mol ethanol (>99.5%) in the presence of  $3.6 \times 10^{-6}$  mol Pluronic F127 triblock copolymer (Sigma, BioReagent). 0.5 ml 0.2 mg  $\text{ml}^{-1}$  colloidal gold solution (XFNANO) was dropped in 50  $\mu\text{l}$  12 M HCl (37 wt%) with the aid of ultrasound for 5 minutes, then mixed with the above Sn precursor solution under constant stirring for overnight.  $\text{Au@SnO}_2/\text{C}_{60}/\text{SnO}_2$  sensing thin films were prepared by spin-coating 40  $\mu\text{l}$  of the Au–Sn precursor solution onto one sensor device with nanocomposite film (Fig. 1 step 2) at 4000 rpm for 60 s under 30% relative humidity for four times, and then dried at 60 °C for 1 h. The sensor device exposed to a water vapour hydrothermal treatment, 95% relative humidity, at 120 °C for 96 h. The final nanocomposite thin films were then oxygen-plasma treated (Femto, 40 kHz, 100 W) for 6 minutes.

### 2.2 Materials characterization

WAXRD data were obtained by a Bruker D8 Advance X-ray diffractometer with  $\text{Cu K}\alpha$  (0.15406 nm) radiation. High



resolution transmission electron microscopy (HRTEM) and scanning transmission electron microscopy in high angle annular dark field mode (STEM-HAADF) were performed using a FEI Titan 80-300 equipped with a field emission gun operated at 300 kV; film parts were scratched from the substrate and collected on an amorphous holey carbon film on a copper grid. Raman spectra were recorded with a LabRAM HR UV-vis (Horiba Jobin Yvon) Raman microscope (Olympus BX41) with a Symphony CCD detection system using a HeNe laser at 632.8 nm. The spectra were taken from material removed from the substrate. The Fourier transform infrared spectra (FTIR) of the samples were recorded on an AVATAR370FT-IR spectrophotometer using conventional KBr pellets.

### 2.3 Sensing measurement

During the sensing measurement, liquid VOCs inputted through a sample inlet and led down to a heater, which vaporized it. A fan ensured that the vapour was homogeneously distributed. The gas sensing properties were determined in a sample cell consists of a sample chamber and has a gas inlet and outlet.<sup>22</sup> A certain concentration of VOCs gas or pure air is periodically passed into the test chamber based on computer-controlled mass flow controllers (MFCs), and the total flow rate is maintained at 1000 sccm. Resistance changes upon sample exposure to gases recorded by a high resistance meter Keithley 6517B. The sensor response is defined as  $R_a/R_g$ , where  $R_a$  and  $R_g$  are the sensor resistances in air and in the target gas, respectively. This parameter is positive for n-type VOCs sensing behaviour. Here, the response or recovery time defined as the time taken for the sensor to achieve 90% of its maximum response or decreases to 10% of its maximum response, respectively.

## 3. Results and discussion

Scanning transmission electron microscopy (STEM) image (Fig. 2a) depicts the structure and morphology of the resulting nanoporous  $\text{Au@SnO}_2/\text{C}_{60}/\text{SnO}_2$  sensing film. It can be seen that there are bigger nanopores with the average diameter of 300 nm exhibiting on the surface of sensing composite film. The pore walls with an average thickness of 160 nm are made up of nanoparticle. The presence of  $\text{C}_{60}$  and Au nanoparticles in the pore wall is further confirmed by the high resolution TEM image (Fig. 2b) showing the region enclosed within the square in upper right of Fig. 2a. The image shows that Au nanoparticles have uniform particle size, and small size of  $\text{SnO}_2$  nanoparticles distributed among Au nanoparticles. The high magnification HRTEM image shows the lattice spacing of 0.33 nm and 0.24 nm, corresponding to the (110) plane of cassiterite phase and (111) plane of gold, respectively. Under these bigger nanopores, the high magnification TEM image (Fig. 2c) of selected region in the lower left of Fig. 2a shows that smaller nanopore arrays are packed in an ordered arrangement with a repeating distance. A fast Fourier transformation of the smaller nanoporous  $\text{SnO}_2$  layer depicted in the insert image of Fig. 2c, indicates orthorhombic symmetry of a [111] oriented

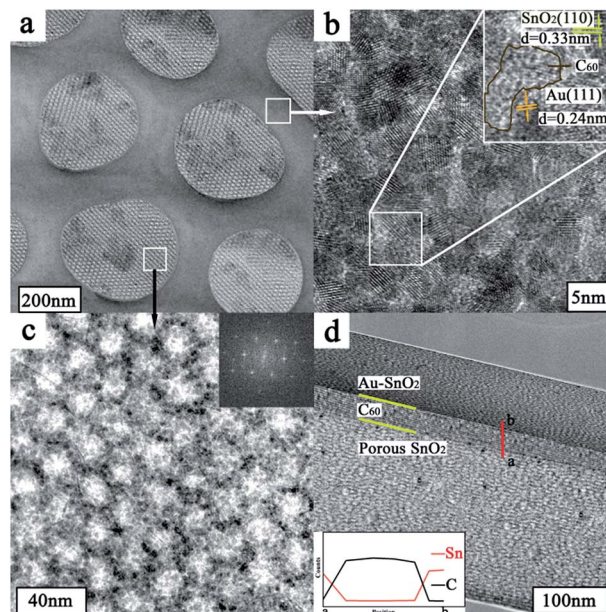


Fig. 2 (a) STEM image of  $\text{Au@SnO}_2/\text{C}_{60}/\text{SnO}_2$  nanocomposite film, (b) HRTEM image shows the region enclosed within the square in upper right of (a). The insert image shows the high magnification of square region in (b). (c) HRTEM image shows the square region in lower left of (a). The insert image shows the fast Fourier transformation of bottom nanoporous  $\text{SnO}_2$  layer. (d) STEM image of cross-section of nanocomposite film. The insert image shows the EDX line measurement of the film.

*Fmmm* nanostructure.<sup>23</sup> It is proved that this sensing film is composed of  $\text{Au@SnO}_2/\text{C}_{60}$  layer covering the surface of ordered nanoporous  $\text{SnO}_2$  layer. The elemental mappings of the nanocomposite film are obtained by energy-dispersive spectroscopy (EDS) for Sn, C, and Au as shown in Fig. S1.† Clearly, C and Au are evenly distributed throughout the  $\text{Au@SnO}_2/\text{C}_{60}$  layer. The STEM image (Fig. 2d) illuminates the cross-section structure of  $\text{Au@SnO}_2/\text{C}_{60}/\text{SnO}_2$  sensing film. Further EDX line measurement taken from the selected area (marked by a red line in Fig. 2d) exhibits the presence of  $\text{C}_{60}$  layer in the composite film, indicating the formation of  $\text{SnO}_2/\text{C}_{60}/\text{SnO}_2$  heterojunctions. Notably, the unique electron coupling at this  $\text{SnO}_2/\text{C}_{60}/\text{SnO}_2$  interface is able to effectively facilitate the electron transfer from the sensing film to integrated electrode.<sup>24</sup>

As shown in Fig. 3a,  $\text{Au@SnO}_2/\text{C}_{60}$  layer is directly grown on ordered nanoporous  $\text{SnO}_2$  thin film using post-synthetic hydrothermal treatment and then oxygen-plasma treated. For further investigating the composite sensing film, the structure and crystallinity of the synthesized thin film are confirmed by X-ray diffraction, FTIR, and Raman studies. Fig. 3b shows the XRD characterization of  $\text{Au@SnO}_2/\text{C}_{60}/\text{SnO}_2$  nanocomposite films prepared by the proposed method. The characteristic peaks of the synthesized nanocomposite films are observed at  $10.7^\circ$ ,  $17.6^\circ$ ,  $20.7^\circ$  and  $27.9^\circ$   $2\theta$  for the  $\text{C}_{60}$  layer. The diffraction peaks at around  $38.3^\circ$  and  $44.5^\circ$  could be indexed to the (111) and (200) planes of a face-centered crystalline structure of Au, respectively. The peaks at  $25.7^\circ$ ,  $33.8^\circ$  and  $51.9^\circ$  are due to the diffraction at the (110), (101) and (211) of  $\text{SnO}_2$ , respectively,



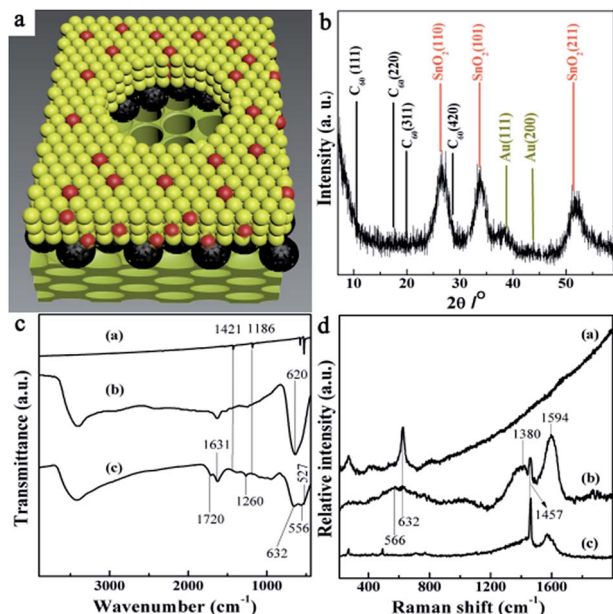


Fig. 3 (a) Schematic illustration of the Au@SnO<sub>2</sub>/C<sub>60</sub>/SnO<sub>2</sub> sensing film. (b) Wide-angle XRD patterns of Au@SnO<sub>2</sub>/C<sub>60</sub>/SnO<sub>2</sub> sensing films. (c) FT-IR spectra of C<sub>60</sub> (a), SnO<sub>2</sub> (b), nanocomposite film (c). (d) Raman spectrum of SnO<sub>2</sub> (a), nanocomposite film (b), and C<sub>60</sub> (c).

indicating the successful formation of cassiterite SnO<sub>2</sub>. The mean crystallite size of the synthesized SnO<sub>2</sub> nanoparticles, which is calculated using Scherrer's formula:  $D_s = 0.9 \times \lambda / (\beta \times \cos \theta)$ , where  $D_s$  is the crystallite size,  $\lambda$  is the wavelength of X-rays ( $\lambda_{\text{Cu}} = 0.15418$  nm),  $\beta$  is the full width at half maximum (FWHM) of the diffraction peak, and  $\theta$  is the Bragg diffraction angle of the XRD peak. The mean crystallite size is 3.1 nm, which is in good agreement with the HRTEM studies (Fig. 2b).

Fig. 3c shows the IR spectra in the range of 400 to 3400 cm<sup>-1</sup> for IR-active fundamental vibrations of C<sub>60</sub> (a), SnO<sub>2</sub> (b), and Au@SnO<sub>2</sub>/C<sub>60</sub>/SnO<sub>2</sub> nanocomposites (c). The peak at 1631 cm<sup>-1</sup> can be attributed to O–H bending vibrations. For Au@SnO<sub>2</sub>/C<sub>60</sub>/SnO<sub>2</sub> nanocomposite films (c), the bands at 527, 577, 1186 and 1421 cm<sup>-1</sup> are attributed to the internal modes of the C<sub>60</sub> molecule. Two new peaks display at 1659 and 1720 cm<sup>-1</sup> for oxygen-plasma treated C<sub>60</sub>, resulting from the stretching vibration of carboxyl groups formed during the treatment. It should be mentioned that these surface functional groups provide active sites for connection with SnO<sub>2</sub> nanocrystals. The IR-active fundamental vibrations of SnO<sub>2</sub> are located in the range of 400–1000 cm<sup>-1</sup>, and the intensive broad bands are ascribed to the stretching vibrations of Sn–O bonds at 556 and 632 cm<sup>-1</sup>. For pure SnO<sub>2</sub> nanoparticle, a broad peak at 621 cm<sup>-1</sup> can be assigned to the vibration of Sn–O. When SnO<sub>2</sub> is modified with C<sub>60</sub>, covalent bonds (e.g., Sn–O–C–O or Sn–O–C) formed due to interaction between oxygen plasma-treated C<sub>60</sub> and SnO<sub>2</sub>. As a result, the main peak associated with SnO<sub>2</sub> slightly red-shift to low frequency, especially for the band at 632 cm<sup>-1</sup>. The IR results further confirm the chemically bonded interaction between C<sub>60</sub> and SnO<sub>2</sub> nanoparticles.

Fig. 3d shows the Raman spectra of SnO<sub>2</sub> (a), the synthesized composite films (b), C<sub>60</sub> (c). For the synthesized composite film

(b), the Raman shifts of C<sub>60</sub> are observed at 265 cm<sup>-1</sup>, 491 cm<sup>-1</sup>, and 1457 cm<sup>-1</sup>, which can be associated with H<sub>1g</sub> squashing, A<sub>1g</sub> breathing, A<sub>2g</sub> pentagonal pinch modes of C<sub>60</sub> molecules, respectively. The two strong peaks located at 1380 cm<sup>-1</sup> (*k*-point phonons of A<sub>1g</sub> symmetry, D-band) and 1594 cm<sup>-1</sup> (E<sub>2g</sub> phonons of C sp<sup>2</sup> atoms, G-band) exhibit that partial C<sub>60</sub> transforms into carbon crystallite in nanocomposite film.<sup>25</sup> Compared to the pure C<sub>60</sub> (c), changes in the relative intensities of the D and G bands (D/G) indicate the changes of the electronic conjugation state of the C<sub>60</sub> during the fabrication procedure. The weak peak located at 632 cm<sup>-1</sup> in nanocomposite film can be assigned to the A<sub>1g</sub> modes of the SnO<sub>2</sub> rutile phase. Besides, the other mode named M<sub>2</sub> (located at 566 cm<sup>-1</sup>) being related to the nano-structure of composite film is also identified in the spectra.<sup>26</sup>

For comparison, we examine the sensing performance of C<sub>60</sub>/SnO<sub>2</sub> film (a), SnO<sub>2</sub>/C<sub>60</sub>/SnO<sub>2</sub> film (b), and Au-functionalized SnO<sub>2</sub>/C<sub>60</sub>/SnO<sub>2</sub> film (c), in terms of the ethanol sensing. The typical response curves of three different SnO<sub>2</sub> based gas sensors being measured at various ethanol concentrations are shown in Fig. 4a. The response, *S*, is defined as  $R_{\text{air}}/R_{\text{gas}}$  for the reducing gases (ethanol) where  $R_{\text{gas}}$  and  $R_{\text{air}}$  denote resistance in the presence and absence of test gases, respectively. The measurements are performed at room temperature with ethanol gas exposure concentration ranging from 0.5 ppm to 50 ppm. A clear increase in the sensor response is observed with increasing gas concentration, and of all the materials tested,

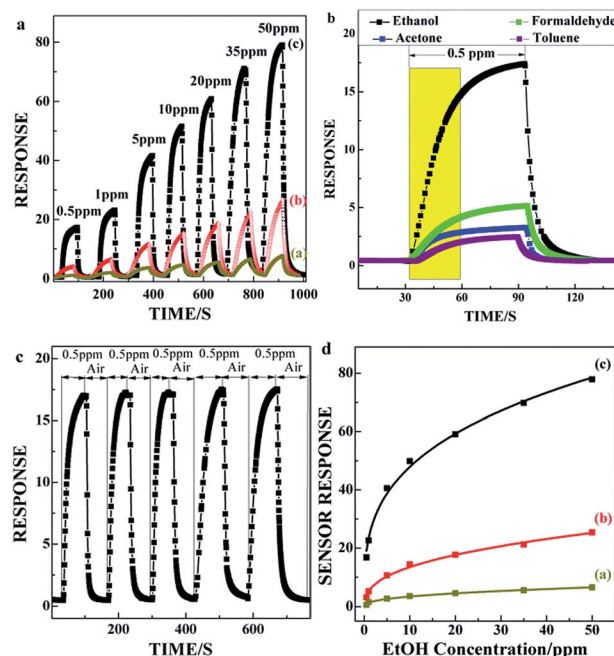


Fig. 4 (a) Responses curves of C<sub>60</sub>/SnO<sub>2</sub> (a), SnO<sub>2</sub>/C<sub>60</sub>/SnO<sub>2</sub> (b), and Au@SnO<sub>2</sub>/C<sub>60</sub>/SnO<sub>2</sub> sensors (c) measured under various ethanol gas concentrations. (b) Typical response and recovery curves of the Au@SnO<sub>2</sub>/C<sub>60</sub>/SnO<sub>2</sub> sensor to different VOCs at 0.5 ppm. (c) Cyclic response changes between air, and 0.5 ppm ethanol in N<sub>2</sub>. (d) Normalized responses of C<sub>60</sub>/SnO<sub>2</sub> (a), SnO<sub>2</sub>/C<sub>60</sub>/SnO<sub>2</sub> (b), and Au@SnO<sub>2</sub>/C<sub>60</sub>/SnO<sub>2</sub> (c) sensors as a function of ethanol gas concentrations.



Au@SnO<sub>2</sub>/C<sub>60</sub>/SnO<sub>2</sub> composite film displays the best ethanol-sensing performance, with high sensor response of 16.8.6 to 0.5 ppm ethanol gas at room temperature.

Moreover, the Au@SnO<sub>2</sub>/C<sub>60</sub>/SnO<sub>2</sub> sensor also depicts the response to formaldehyde, acetone, and toluene gases, as shown in Fig. 4b. The 0.5 ppm ethanol response (16.8) becomes more than four times as high as that of formaldehyde. Thus, the Au@SnO<sub>2</sub>/C<sub>60</sub>/SnO<sub>2</sub> sensor reveals not only high response but also high ethanol selectivity at low concentration. The response curves illuminate excellent stability, as shown in Fig. 4c. The response time defined as the time necessary to reach 90% of the maximum response is about 35 s, and the recovery time is about 9 s. In Fig. 4d, the Au@SnO<sub>2</sub>/C<sub>60</sub>/SnO<sub>2</sub> gas sensor (c) shows a power law relationship between  $S$  and  $C_{\text{EtOH}}$ , and the correlation coefficient ( $n$ ) is estimated to be 0.31 within the gas concentration ranging from 0.5 to 50 ppm ( $S = a \times C^n$ ). They are determined by n/p/n heterostructure in the nanoporous structure which strongly influences carrier mobility in the sensing film. The high sensitivity of Au@SnO<sub>2</sub>/C<sub>60</sub>/SnO<sub>2</sub> sensor may be due to the high reactivity of ethanol with adsorbed oxygen in the presence of Au-sites on the SnO<sub>2</sub>/C<sub>60</sub>/SnO<sub>2</sub> surface. The quick response and recovery would also be attributed to the nanoporous structure and n/p/n heterostructure of the composite film. Fig. S2† exhibits the long-term stability of the Au@SnO<sub>2</sub>/C<sub>60</sub>/SnO<sub>2</sub> sensor exposed to 0.5 ppm ethanol gas. The stability of the sensor is measured over different times on stream. The average and relative standard deviation of the response ( $S$ ) of the ethanol gas sensor at a testing concentration of 0.5 ppm of ethanol for 48 days are 16.8 and 1.1%, respectively.

The generation of n/p/n heterojunctions (Fig. 5a) can inevitably develop the depletion regions of both sides of junctions, decreasing the conduction volume of SnO<sub>2</sub> nanoparticles. The introduction/removal of ethanol gas will induce the more significant change of conduction volume in case of SnO<sub>2</sub>/C<sub>60</sub>/SnO<sub>2</sub> composite films. This will bring about the larger change in resistance, enhancing the sensitivity. Fig. 5b schematically depicts the changes of the electronic energy bands for C<sub>60</sub>/SnO<sub>2</sub> material before and after the adsorption of ethanol gases. This figure shows two depletion layers—one is on the surface of the SnO<sub>2</sub> nanoparticles, and the other is in the interface between C<sub>60</sub> and SnO<sub>2</sub> nanoparticles. In the n/p/n heterojunctions, the work function of n-SnO<sub>2</sub> and C<sub>60</sub> are 4.55 and 4.72 eV,<sup>27</sup> respectively. Due to the charge transfer, the potential barrier (0.17 eV) will be developed at heterojunctions, being accompanied by the bending of the vacuum energy level and the energy band. The local p/n heterojunctions between C<sub>60</sub> and SnO<sub>2</sub> nanoparticles will provide additional modulation of resistance during the introduction and removal of ethanol gas by changing the heterojunction barrier.

In case of Au, Au being a better oxygen dissociation catalyst than SnO<sub>2</sub> enhances the rate of dissociation and diffusion of oxygen species on the surface of SnO<sub>2</sub>, resulting in a greater degree of electron withdrawal from the conduction band of SnO<sub>2</sub> ("spill-over" effect). In the Au/SnO<sub>2</sub> heterojunctions (Fig. 5c), the work function of Au (5.1 eV) is larger than that of SnO<sub>2</sub> (4.55 eV). In order to align the Fermi level, the electrons will flow from SnO<sub>2</sub> to Au sides, as the electrostatic potential of

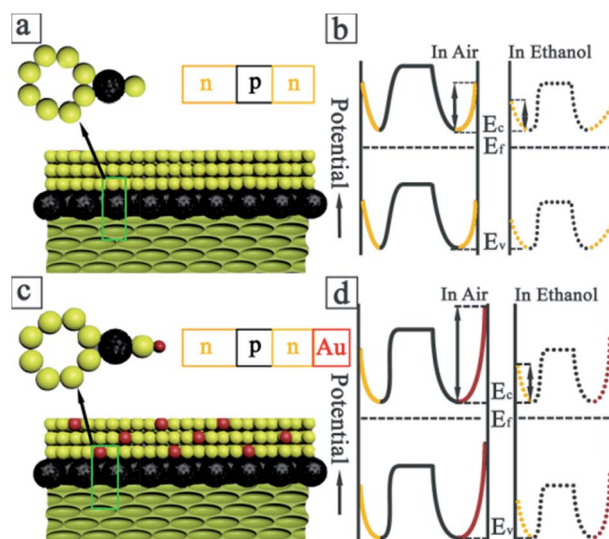


Fig. 5 (a) Schematic illustration of the SnO<sub>2</sub>/C<sub>60</sub>/SnO<sub>2</sub> sensing film. (b) Potential barrier to electronic conduction at grain boundary for SnO<sub>2</sub>/C<sub>60</sub>/SnO<sub>2</sub> sensing film. (c) Schematic illustration of the Au@SnO<sub>2</sub>/C<sub>60</sub>/SnO<sub>2</sub> sensing film. (d) Potential barrier to electronic conduction at grain boundary for Au@SnO<sub>2</sub>/C<sub>60</sub>/SnO<sub>2</sub> sensing film.

the semiconductor is increased. Being similar to the C<sub>60</sub>-SnO<sub>2</sub> heterojunctions, the Schottky barriers (0.55 eV) generated at Au-SnO<sub>2</sub> heterojunctions will provide additional modulation of resistance during the adsorption and desorption of gas molecules by changing the heterojunction barrier. In equilibrium and in the absence of ethanol gas, because the Au work function is large, a depletion layer will be developed in the SnO<sub>2</sub> nanoparticle. For Au with high work function, this depletion region of electrons is much more pronounced, which gives rise to a larger barrier height. This manifests a larger electrical resistance of the sensing film in air, as shown in Fig. 5d.

From Fig. 5b, we can see that Au@SnO<sub>2</sub>/C<sub>60</sub>/SnO<sub>2</sub> nanocomposite sensor shows far greater sensitivity to ethanol gas than other gases, manifesting the excellent selectivity to ethanol. On the one hand, it is reported that the O-H band of ethanol is important for the adsorption onto the SnO<sub>2</sub> (110) surface. And the SnO<sub>2</sub> (110) surface is highly sensitive to ethanol due to its powerful attraction to the polar O-H bond. Even more, quantum size SnO<sub>2</sub> nanoparticles (3.1 nm) can provide a catalytic effect to decrease the activation energy of ethanol to oxidize and decompose by first weakening the O-H bond of the ethanol molecule at room temperature.<sup>28</sup> On the other hand, the Au-functionalized SnO<sub>2</sub>/C<sub>60</sub>/SnO<sub>2</sub> sensor exhibits an extreme selectivity to ethanol, in comparison to other gases such as toluene. Adsorbed phenyl groups are stable on the surface until 165 K, but the chemisorbed phenyl group will be desorbed from the Au surface at room temperature. With the reasonable assumption that the stable adsorption is the primarily crucial step for subsequent catalytic reactions, Au NPs will provide both high sensitivity and selectivity in sensing ethanol in comparison to toluene at room temperature.<sup>29</sup>

Up to the present, significant amount of research work has been reported on the sensing of ethanol gas (Table S1†). First,



high sensor responses were attained by means of using various materials systems, including SnO<sub>2</sub>-ZnO core-shell nanowires,<sup>30</sup> Pt@SnO<sub>2</sub> nanorods,<sup>1</sup> ZnO/MWNTs nanocomposite films,<sup>31</sup> C<sub>3</sub>N<sub>4</sub> nanosheet modified SnO<sub>2</sub>,<sup>32</sup> noble metal@metal oxide semiconductors core@shell nanoarchitectures,<sup>3</sup> SnO<sub>2</sub>-RGO hybrid composite films.<sup>10,33,34</sup> Accordingly, there are rare reports on the preparation of highly sensitive ethanol sensor operating at room temperature below 1 ppm. Wu *et al.* have investigated the sensing activity of Ag@SnO<sub>2</sub> core@shell NPs for ethanol by comparing its gas sensing performance with bare SnO<sub>2</sub> nanomaterials. The sensor response of core@shell NPs was 0.3 and the response and recovery times of 34 s and 68 s at room temperature.<sup>35</sup> Li *et al.* utilized Au-decorated SnO<sub>2</sub> nanoparticles for obtaining the higher response of 0.6 at a low concentration of 0.5 ppm.<sup>36</sup> However, the grain size was more than 30 nm, which hindered the further improvement in sensing performance. In this work, the gas sensor exhibits ultrahigh sensitivity to ethanol gas with response value up to 16.8 to 0.5 ppm at room temperature.

## 4. Conclusions

In summary, we employ not only the Au-functionalization but also the C<sub>60</sub>-functionalization to synthesize hierarchically nanoporous composite films for enhancing the sensing performance. The fabricated hierarchically nanoporous Au@SnO<sub>2</sub>/C<sub>60</sub>/SnO<sub>2</sub> nanocomposite are obtained through water vapour hydrothermal treatment and layer by layer self-assembly. Their hierarchical nanopore structure is bimodal with closely packed open macropores (~300 nm) at Au@SnO<sub>2</sub>/C<sub>60</sub> layer and with highly ordered nanoporous with a narrow size range of nanopores mainly from 8–10 nm at the bottom SnO<sub>2</sub> layer. The structure, crystallinity and composition of the hierarchical structure Au@SnO<sub>2</sub>/C<sub>60</sub>/SnO<sub>2</sub> nanocomposite films are characterized by XRD, Raman, HRTEM, and SAED. Interestingly, the Au@SnO<sub>2</sub>/C<sub>60</sub>/SnO<sub>2</sub> nanocomposite films are treated with oxygen-plasma treatment to remove the organic template and modify the sensing activity. The Au@SnO<sub>2</sub>/C<sub>60</sub>/SnO<sub>2</sub> nanocomposite sensor demonstrates the ultrasensitive ethanol sensing behaviour at room temperature. The sensing properties of Au@SnO<sub>2</sub>/C<sub>60</sub>/SnO<sub>2</sub> nanocomposite sensors are investigated by exposing it to ethanol gas with a concentration range from 0.5 ppm to 50 ppm. Furthermore, these gas sensors exhibit ultrahigh sensitivity to ethanol gas with response value up to 16.8 to 0.5 ppm and a short recovery time of 9 second at room temperature. The synthesis method of combining the hierarchical nanoporous structure with layer by layer self-assembly is a general technique, and offers a promising strategy for preparing high performance nanoporous crystalline materials for applications including gas sensing, photocatalysis, and 3<sup>rd</sup> generation photovoltaics.

## Conflicts of interest

There are no conflicts to declare.

## Acknowledgements

This work was supported by the Start up Foundation for Introducing Talent of NUIST (2014r034), Project of Natural Science Foundation of the Higher Education Institutions of Jiangsu Province (17KJB430024) and Horizontal Subject (2016h036).

## References

- 1 X. Xue, Z. Chen, C. Ma, L. Xing, Y. Chen, Y. Wang and T. Wang, *J. Phys. Chem. C*, 2010, **114**, 3968.
- 2 B. Zhang, W. Fu, H. Li, X. Fu, Y. Wang, H. Bala, X. Wang, G. Sun, J. Cao and Z. Zhang, *Appl. Surf. Sci.*, 2016, **363**, 560.
- 3 P. Rai, S. M. Majhi, Y.-T. Yu and J.-H. Lee, *RSC Adv.*, 2015, **5**, 76229.
- 4 S. Shao, R. Koehn, H. Wu, T. Wu and W.-F. Rao, *New J. Chem.*, 2016, **40**, 5523.
- 5 X. Sun, H.-t. Fang, H.-l. Yu, Y. Chu, B.-y. Zhang, J.-h. Du, D.-w. Wang, F. Li and F.-p. Wang, *New Carbon Mater.*, 2010, **25**, 218.
- 6 S. Salehi, E. Nikan, A. A. Khodadadi and Y. Mortazavi, *Sens. Actuators, B*, 2014, **205**, 261.
- 7 P. Baraneedharan, S. Alexander and S. Ramaprabhu, *J. Appl. Electrochem.*, 2016, **46**, 1187.
- 8 M. Mazloum-Ardakani and A. Khoshroo, *Electrochem. Commun.*, 2014, **42**, 9.
- 9 J. A. Rather, A. J. A. Harthi, E. A. Khudaish, A. Qurashi, A. Munama and P. Kannan, *Anal. Methods*, 2016, **8**, 5690.
- 10 C. A. Zito, T. M. Perfecto and D. P. Volanti, *Sens. Actuators, B*, 2017, **244**, 466.
- 11 Y. Qu, H. Wang, H. Chen, M. Han and Z. Lin, *Sens. Actuators, B*, 2016, **228**, 595.
- 12 Q. T. Minh Nguyet, N. Van Duy, N. T. Phuong, N. N. Trung, C. M. Hung, N. D. Hoa and N. Van Hieu, *Sens. Actuators, B*, 2017, **238**, 1120.
- 13 P. Clément, S. Korom, C. Struzzi, E. J. Parra, C. Bittencourt, P. Ballester and E. Llobet, *Adv. Funct. Mater.*, 2015, **25**, 4011.
- 14 A. Wittstock, J. Biener and M. Baumer, *Phys. Chem. Chem. Phys.*, 2010, **12**, 12919.
- 15 S. Arunkumar, T. Hou, Y.-B. Kim, B. Choi, S. H. Park, S. Jung and D.-W. Lee, *Sens. Actuators, B*, 2017, **243**, 990.
- 16 C. Liu, H. Tai, P. Zhang, Z. Ye, Y. Su and Y. Jiang, *Sens. Actuators, B*, 2017, **246**, 85.
- 17 N. Goswami, F. Lin, Y. Liu, D. T. Leong and J. Xie, *Chem. Mater.*, 2016, **28**, 4009.
- 18 Y. Liu, Y. Zheng, B. Du, R. R. Nasaruddin, T. Chen and J. Xie, *Ind. Eng. Chem. Res.*, 2017, **56**, 2999.
- 19 J. Li, T. Zhao, T. Chen, Y. Liu, C. N. Ong and J. Xie, *Nanoscale*, 2015, **7**, 7502.
- 20 Y. Liu, Q. Yao, X. Wu, T. Chen, Y. Ma, C. N. Ong and J. Xie, *Nanoscale*, 2016, **8**, 10145.
- 21 F. Gu, H. Wang, D. Han and Z. Wang, *Sens. Actuators, B*, 2017, **245**, 1023.
- 22 S. Shao, H. Wu, S. Wang, Q. Hong, R. Koehn, T. Wu and W.-F. Rao, *J. Mater. Chem. C*, 2015, **3**, 10819.
- 23 C. Boissiere, D. Grosso, S. Lepoutre, L. Nicole, A. B. Bruneau and C. Sanchez, *Langmuir*, 2005, **21**, 12362.



- 24 Z. Zhu, Y. Bai, X. Liu, C. C. Chueh, S. Yang and A. K. Jen, *Adv. Mater.*, 2016, **28**, 6478.
- 25 Y. Qu, H. Wang, H. Chen, M. Han and Z. Lin, *Sens. Actuators, B*, 2016, **228**, 595.
- 26 F. H. Aragón, J. C. R. Aquino, N. C. S. Gomes, J. D. Ardisson, S. W. da Silva, D. G. Pacheco-Salazar and J. A. H. Coaquira, *J. Eur. Ceram. Soc.*, 2017, **37**, 3375.
- 27 H. Liang, S. Xu, W. Liu, Y. Sun, X. Liu, X. Zheng, S. Li, Q. Zhang, Z. Zhu, X. Zhang, C. Dong, C. Li, G. Yuan and H. Mimura, *Phys. Lett. A*, 2013, **377**, 2676.
- 28 J. Yue, X. Jiang and A. Yu, *J. Phys. Chem. C*, 2013, **117**, 9962.
- 29 D. Syomin, J. Kim, B. E. Koel and G. B. Ellison, *J. Phys. Chem. B*, 2001, **105**, 8387.
- 30 D. T. Thanh Le, D. D. Trung, N. D. Chinh, B. T. Thanh Binh, H. S. Hong, N. Van Duy, N. D. Hoa and N. Van Hieu, *Curr. Appl. Phys.*, 2013, **13**, 1637.
- 31 D. Zhang, Y. e. Sun and Y. Zhang, *J. Mater. Sci.: Mater. Electron.*, 2015, **26**, 7445.
- 32 J. Cao, C. Qin, Y. Wang, H. Zhang, B. Zhang, Y. Gong, X. Wang, G. Sun, H. Balac and Z. Zhang, *RSC Adv.*, 2017, **7**, 25504.
- 33 D. Zhang, J. Liu, H. Chang, A. Liu and B. Xia, *RSC Adv.*, 2015, **5**, 18666.
- 34 J.-H. Kim, A. Katoch, H. W. Kim and S. S. Kim, *Chem. Commun.*, 2016, **52**, 3832.
- 35 R.-J. Wu, D.-J. Lin, M.-R. Yu, M. H. Chen and H.-F. Lai, *Sens. Actuators, B*, 2013, **178**, 185.
- 36 Y. Li, F.-X. Zhao, X.-X. Lian, Y.-L. Zou, Q. Wang and Q.-J. Zhou, *J. Electron. Mater.*, 2016, **45**, 3149.

